


## Hot-electron deposition and implosion mechanisms within electron shock ignition

Wan-Li Shang(尚万里), Xing-Sen Che(车兴森), Ao Sun(孙奥), Hua-Bing Du(杜华冰), Guo-Hong Yang(杨国洪), Min-Xi Wei(韦敏习), Li-Fei Hou(侯立飞), Yi-Meng Yang(杨轶濛), Wen-Hai Zhang(张文海), Shao-Yong Tu(涂绍勇), Feng Wang(王峰), Hai-En He(何海恩), Jia-Min Yang(杨家敏), Shao-En Jiang(江少恩), Bao-Han Zhang(张保汉)

**Citation:**Chin. Phys. B . 2020, 29(10): 105201 . **doi:** 10.1088/1674-1056/aba9c3
Journal homepage: http://cpb.iphy.ac.cn; http://iopscience.iop.org/cpb

**What follows is a list of articles you may be interested in**

---

## Suppression of auto-resonant stimulated Brillouin scattering in supersonic flowing plasmas by different forms of incident lasers

S S Ban(班帅帅), Q Wang(王清), Z J Liu(刘占军), C Y Zheng(郑春阳), X T He(贺贤土)

Chin. Phys. B . 2020, 29(9): 095202 . **doi:** 10.1088/1674-1056/ab9c12

## Influence analysis of symmetry on capsule in six-cylinder-port hohlraum

You Zou(邹游), Wudi Zheng(郑无敌), Xin Li(李欣)

Chin. Phys. B . 2019, 28(3): 035203 . **doi:** 10.1088/1674-1056/28/3/035203

## Rayleigh-Taylor instability at spherical interfaces of incompressible fluids

Hong-Yu Guo(郭宏宇), Li-Feng Wang(王立锋), Wen-Hua Ye(叶文华), Jun-Feng Wu(吴俊峰), Ying-Jun Li(李英骏), Wei-Yan Zhang(张维岩)

Chin. Phys. B . 2018, 27(2): 025206 . **doi:** 10.1088/1674-1056/27/2/025206

## A new ignition hohlraum design for indirect-drive inertial confinement fusion

Xin Li(李欣), Chang-Shu Wu(吴畅书), Zhen-Sheng Dai(戴振生), Wu-Di Zheng(郑无敌), Jian-Fa Gu(谷建法), Pei-Jun Gu(古培俊), Shi-Yang Zou(邹士阳), Jie Liu(刘杰), Shao-Ping Zhu(朱少平)

Chin. Phys. B . 2016, 25(8): 085202 . **doi:** 10.1088/1674-1056/25/8/085202

## Diagnostic technique for measuring fusion reaction rate for inertial confinement fusion experiments at Shen Guang-III prototype laser facility

Wang Feng, Peng Xiao-Shi, Kang Dong-Guo, Liu Shen-Ye, Xu Tao

Chin. Phys. B . 2013, 22(11): 115204 . **doi:** 10.1088/1674-1056/22/11/115204

---

# Hot-electron deposition and implosion mechanisms within electron shock ignition*

Wan-Li Shang(尚万里)†, Xing-Sen Che(车兴森), Ao Sun(孙奥), Hua-Bing Du(杜华冰), Guo-Hong Yang(杨国洪), Min-Xi Wei(韦敏习), Li-Fei Hou(侯立飞), Yi-Meng Yang(杨轶濛), Wen-Hai Zhang(张文海), Shao-Yong Tu(涂绍勇), Feng Wang(王峰), Hai-En He(何海恩), Jia-Min Yang(杨家敏), Shao-En Jiang(江少恩), and Bao-Han Zhang(张保汉)

*Research Center of Laser Fusion, China Academy of Engineering Physics, Mianyang* 621900, *China*

(Received 1 June 2020; revised manuscript received 12 July 2020; accepted manuscript online 28 July 2020)

A hot-electron driven scheme can be more effective than a laser-driven scheme within suitable hot-electron energy and target density. In our one-dimensional (1D) radiation hydrodynamic simulations, 20× pressure enhancement was achieved when the ignitor laser spike was replaced with a 60-keV hot-electron spike in a shock ignition target designed for the National Ignition Facility (NIF), which can lead to greater shell velocity. Higher hot-spot pressure at the deceleration phase was obtained owing to the greater shell velocity. More cold shell material is ablated into the hot spot, and it benefits the increases of the hot-spot pressure. Higher gain and a wider ignition window can be observed in the hot-electron-driven shock ignition.

**Keywords:** shock ignition, inertial confinement fusion, hot electron, plasma fusion

**PACS:** 52.58.–c, 52.57.–z, 81.15.Jj, 89.30.Jj **DOI:** 10.1088/1674-1056/aba9c3

## 1. Introduction

Recent theoretical and experimental results have suggested that launching a spherically convergent shock wave at the end of the acceleration phase improves the ignition conditions for inertial confinement fusion (ICF) implosions.[1,2] Such an ICF scheme with a late shock is referred to as "shock ignition".[3–6] The shock ignition is a scheme that is based on the principles of conventional central hot-spot ignition and uses a late shock to augment the compression of the central hot spot above the ignition threshold. The maximum hot-spot pressure is achieved when the outcoming return shock driven by the high central pressure of the collapsing capsule collides, near the inner shell interface, with the incoming ignitor shock launched after the end of acceleration phase.[7,8] The ignitor shock can be launched by a spike in the laser power or by energetic particles.[9] The latter can be generated by a high-intensity laser pulse used to accelerate electrons in the coronal plasma.[10–12] In principle, laser-driven hot electrons can be very efficient in driving the ignitor shock if their stopping range is small in comparison with the target thickness at the shock launching time. For convenience, we will make a distinction between the case of a shock driven hydrodynamically and the case of a shock driven by energetic particles. The hydrodynamic drive is the conventional process for driving a shock through a spike in the laser power.[13] The laser energy deposited during the power spike drives a thermal wave toward the ablator surface, resulting in higher ablation and stronger ram pressure. The ram pressure drives the shock hydrodynamically. If a burst of energetic particles is used, the temperature and pressure of the shell increase where the particle energy is deposited. The high pressure resulting from the particle heating drives the shock. If the energetic particles are produced by a high-intensity laser pulse, it is then also possible to develop a mixed shock with a hydrodynamic drive as well as a particle drive. Depending on the direction of the energetic particles and their energy, the particle drive could, in principle, be more effective than the hydrodynamic drive and produce stronger ignitor shocks.

In a shock-ignition implosion, the main pulse used to assemble the dense core is a conventional low-adiabat laser pulse and the target is typically a thick cryogenic shell.[14] Thick, massive shells can produce high energy gains because of the large amounts of thermo-nuclear fuel. Because of their large mass, thick shells are driven at low implosion velocities and require very large drivers to trigger conventional hot-spot ignition. Indeed, the laser energy required for conventional hot-spot ignition is a strong function of the implosion velocity $E_{\rm L}^{\rm ign} \sim V_{\rm i}^{-6.6}$.[14] The greater the shell mass, the lower the velocity and the larger the laser energy required for ignition. By launching a shock at the end of the main laser pulse, the hot-spot pressure is significantly enhanced and the energy required for ignition is decreased by the factor $\Phi \approx (p_{\rm shock}/p_{\rm noshock})^3$, where $p_{\rm shock}$ is the hot-spot pressure enhanced by the shock and $p_{\rm noshock}$ is the hot-spot pressure without the shock.[3] It was found that a hydrodynamically driven shock can lead to a pressure increase of $\sim$ 50% to 70%, thereby resulting in a

*Project supported by the National Natural Science Foundation of China (Grant No. 11775203) and the Presidential Foundation of China Academy of Engineering Physics (Grant No. YZJJLX 2016007).

†Corresponding author. E-mail: wanlishang@gmail.com

© 2020 Chinese Physical Society and IOP Publishing Ltd 

3× to 5× reduction in the energy required for ignition. It is important to emphasize that such an ignition energy reduction applies to hydrodynamic equivalent implosions. As explained in the available work,[15] hydrodynamically equivalent implosions have the same implosion velocity, adiabat laser intensity, and in-flight aspect ratio (IFAR). Rather than using a late shock, one can reduce the energy required for ignition by increasing the implosion velocity. This can be accomplished by either increasing the laser energy on target or reducing the target mass. The same 3× to 5× reduction in the energy required for ignition from a late shock can be accomplished by an increase of 18% to 27% in the implosion velocity. However, raising the implosion velocity leads to a significant enhancement in the hydrodynamic instability growth since the IFAR would increase by 40% to 60%.

An even larger enhancement of the hot-spot pressure can be achieved if the late shock is driven by energetic particles, which is called "electron shock ignition".[9] This can occur when a significant portion of the laser energy used to drive the ignitor shock is used to generate hot electrons that slow down on the shell's outer surface. As shown later in this paper, if the conversion of laser energy into incident hot electrons exceeds ∼ 10%, the increase in ignitor shock strength can ignite an implosion. In this case, most of the hot-spot energy comes from the ignitor shock, and even very low velocity targets can be ignited by the ignitor shock compression. High gain and robust ignition are obtained with electron shock ignition.[9] In this work, the detailed hot-electron energy deposition and implosion physics of electron shock ignition are discussed.

## 2. Hot electron energy deposition

Kilo-electron-Volt (keV) energetic electrons can be generated by the nonlinear precess of laser plasma interactions, including the three-wave parametric instabilities (LPI): stimulated Raman scattering (SRS), two plasmon decay (TPD), and filamentation instability, when the laser intensity is around $5\times10^{14}$ W/cm$^2$ to $2\times10^{15}$ W/cm$^2$ for conventional direct- and indirect-drive (ICF).[16,17] When laser intensity increases up to $10^{18}$ W/cm$^2$ for fast ignition, other LPI schemes like relativistic interaction regime occur owing to the high laser normalized vector potential, and MeV energetic electrons are produced to drive the implosion.[18] As for the shock-ignition laser intensity $2\times10^{15}$ W/cm$^2$–$10^{16}$ W/cm$^2$, recent OMEGA experiment data show that the hot electrons are produced by an LPI like SRS and can carry up to ∼15% of the laser energy.[19] Megajoule-scale targets will likely produce even more hot electrons because of the larger plasma scale length since the plasma scale length can be written as $L = c_s t$, where $c_s$ is the ion sound speed at the critical surface and $t$ is the duration of the laser pulse.

The energy deposition of energetic electrons in plasmas has been widely studied.[10–12,20,21] An analytical model of ablation pressure formation and shock-wave propagation driven by an energetic electron beam was developed and confirmed with numerical simulations.[10] A self-similar isothermal rarefaction wave model was utilized to investigate the expanding plasma, and the formation of a shock wave in the target under the expanding plasma is described in Ref. [11]. It was found that the intense electron produced ablation pressure does not depend on the plasma temperature but only on the plasma density and electron energy, and the maximum ablation pressure (in unit Mbar, the unit 1 bar $= 10^5$ Pa) can be described as $P = 175\rho^{1/3}(I_{15}\eta)^{2/3}$, where $\rho$ is the material density in units of g/cm$^3$, and $\eta$ is the conversion efficiency of laser energy to hot-electron energy. The relationship of the electron temperature and the laser intensity on the generation of high pressure has been studied.[12] A stopping power model was built that can be used in theoretical studies of the ignition conditions and particle-in-cell (PIC) and Monte Carlo simulations of the collisional electron transport in the plasma.[20] The interaction of directed energetic electrons with hydrogenic and arbitrary-Z plasmas has been analytically modeled.[21] The effects of stopping, straggling, and beam blooming, a consequence of scattering, and energy loss, are rigorously treated from a unified approach.[21]

The Maxwellian distribution of hot electrons is widely used.[22,23] In our work, we adopt the Maxwellian distribution for hot-electron energy with an expression of $f(E) = 1/A\,\mathrm{e}^{E/T}$, where $E$ is the energy of the monoenergic hot electron, $f(E)$ is the distribution function, the parameter $A$ is the undetermined coefficient, which will be set according to the hot-electron energy, and $T$ is the hot-electron temperature. Fifty group energy zones were used up to 400 keV; the hot electron distributions for 40 keV, 60 keV, and 100 keV are shown in Fig. 1.

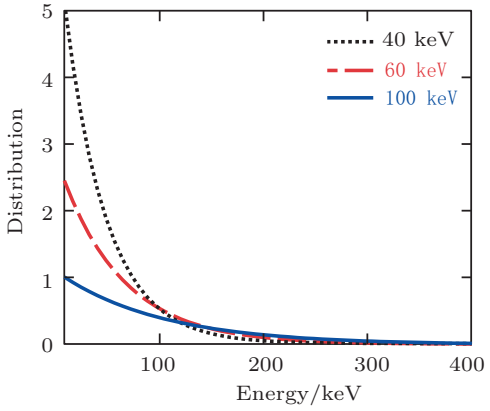



**Fig. 1.** The normalized Maxwellian distribution of hot-electron temperature of 40 keV, 60 keV, and 100 keV.

The accurate calculations of hot-electron transport and energy deposition are PIC and Monte Carlo simulations. Most Monte Carlo codes use tables for the electron stopping power

and transport scattering cross sections obtained for normalized media[20] to investigate the scattering of fast electrons by plasma electrons and ions, but it is very expensive for them to be adopted in hydrodynamic simulations. In this work, to put a hot-electron transport and energy deposition package into an available hydrocode DEC2D,[9,24–26] the hot-electron stopping power model built by Solodov and Betti[20] is utilized. DEC2D is a two-dimensional (2D) eulerian radiation–hydrodynamics code. Essential physics like two fluids, thermal transport, radiation, and alpha diffusion are included in this code. A moving mesh scheme is utilized that shrinks radially with the average velocity and maintains a high resolution throughout the convergence. DEC2D is developed to simulate the deceleration phase of an ICF implosion with perturbations, and 1D calculations are performed in this work.

In the Solodov–Betti model, the cross sections for fast electrons scattering off plasma ions and electrons are obtained in the first Born approximation.[20] Binary collisions including electron–electron and electron–ion collisions are considered, and the individual stopping power by binary collisions is analyzed. Apart from binary collisions, fast electrons lose their energy in plasma by exciting plasma waves. Individual-particle behavior and collective behavior such as plasma oscillations are taken into consideration and depend on the comparison of the dimension to the Debye screening distance. The total stopping power can be written as

$$\frac{\mathrm{d}E}{\mathrm{d}s} = -\frac{2\pi r_0^2 mc^2 n_\mathrm{e}}{\beta^2}\left\{\ln\left[\left(\frac{E}{2\hbar\omega_\mathrm{p}}\right)^2\frac{\gamma+1}{\gamma^2}\right]+1+\frac{1}{8}\left(\frac{\gamma-1}{\gamma}\right)^2\right\}, \tag{1}$$

where $r_0$ is the classical electron radius, $m$ is the electron mass, $c$ is the vacuum light velocity, $n_\mathrm{e}$ is the electron density, $\beta$ is the electron velocity normalized to $c$, $E$ is the hot-electron energy, $\hbar\omega_\mathrm{p}$ is the plasmon energy, and $\gamma = (1-\beta^2)^{-0.5}$.

The target used in our work was taken from the 1D hydrocode LILAC target design for NIF shock ignition.[27] A massive 1080-μm-outer-radius, 192-μm-thick plastic capsule is driven by the UV laser pulse. The pulse shape consists of an adiabat-shaping[28] assembly pulse with two pickets setting the shell on an inner adiabat $\alpha \sim 1.8$ at the ignitor spike launching time, and a shell implosion velocity $V_\mathrm{i} \sim 200$ km/s. The compressed target without an ignitor spike is simulated. The radial profiles of density, pressure, velocity, and temperature are extracted from LILAC calculations. Hot-electron transport and energy deposition with different monoenergetic hot electrons are shown in Fig. 2. The plasma density profile also shown in Fig. 2, is extracted from the above target design at 10.2 ns. For the 40-, 60-, and 100-keV monoenergetic hot electrons, the plasma at 10.2 ns is massive enough to stop the hot electrons at the outside shell surface. According to the stopping power model,[20]

$$\rho\langle x\rangle = \frac{0.82E^2}{0.44+E}\left(\frac{\rho}{300}\right)^{0.07}\left(\frac{T}{5}\right)^{-0.02},$$

the hot-electron propagation range is most dependent on the hot-electron energy, which implies that a higher-energy-hot-electron leads to a greater propagation range and is consistent with those demonstrated in Fig. 2. Abrupt shock-front surfaces are formed, because at the outside surface of the shell, the plasma density increases as the hot electron propagates, which results in more energy deposition as the hot electron transports. Similar profiles of shocks generated by hot electron energy deposition have been observed by analytical model and simulation.[11]

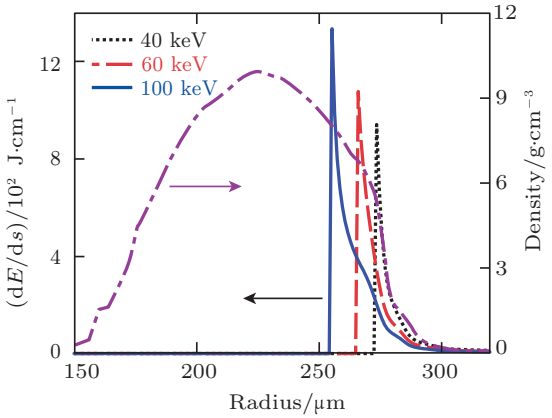



**Fig. 2.** The energy depositions (solid lines) for the monoenergetic hot electrons with energies of 40 keV, 60 keV, and 100 keV. The density profile is shown as the dashed line.

The integro-differential diffusion equation of the multiple scattering problem in an infinite, homogeneous plasma was studied.[29] It was suggested that the spatial moments of the electron-distribution function can be expressed through the mean values of the spherical harmonics.[20,29] A simple formula about the spatial moments of the electron-distribution function can be obtained as

$$\langle\cos\theta\rangle \approx \left[\frac{(\gamma-1)/(\gamma+1)}{(\gamma_0-1)/(\gamma_0+1)}\right]^{Z\alpha}, \tag{2}$$

where $Z$ is the ionized degree, and $\alpha$ can be written as

$$\alpha = \frac{\ln\Lambda^{\mathrm{ei}} + Z^{-1}\ln\Lambda^{\mathrm{ee}} + 1 + Z^{-1}}{\lambda^{\mathrm{ene}}} \tag{3}$$

where $\ln\Lambda^{\mathrm{ei}}$ and $\ln\Lambda^{\mathrm{ee}}$ are Coulomb logarithms. The spatial moments of the electron-distribution function from Eq. (2) was calculated and shown in Fig. 3 with three different monoenergetic hot-electron energies of 40, 60, and 100 keV. The plasma density profile is the same as that in Fig. 2. With higher plasma density, the mean free path of the hot electron is less, which

leads to more collision and scattering with both electrons and ions, and then a larger scattering angle arises. As a result, a smaller $\langle\cos\theta\rangle$ happens with higher plasma density, which is consistent with that shown in Fig. 3. Equations (1)–(3) can be used to calculate the stopping power in the direction of the initial electron velocity

$$\frac{\mathrm{d}E}{\mathrm{d}x} = \langle\cos\theta\rangle^{-1}\frac{\mathrm{d}E}{\mathrm{d}s}. \tag{4}$$

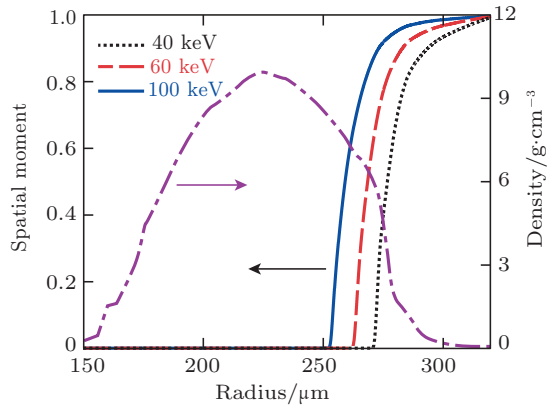



**Fig. 3.** The spatial moments (solid lines) of the electron-distribution function for the monoenergetic hot electrons with energies of 40 keV, 60 keV, and 100 keV. The density profile is shown as the dashed line.

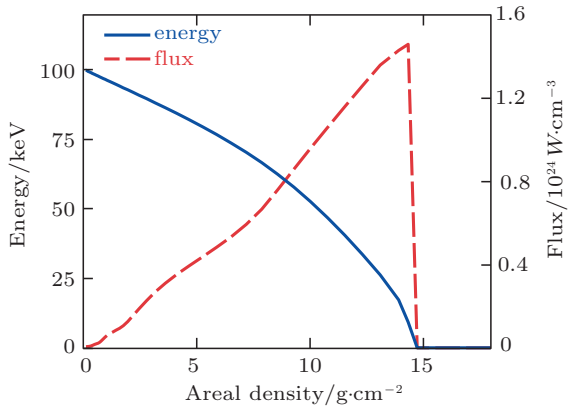



**Fig. 4.** The energy deposition (blue line) and the locally deposited flux (red line) of the 100-keV monoenergetic hot electron in DT plasma.

A hot-electron transport and energy deposition package is developed according the above model and put into hydrocode DEC2D. Within DT plasma ($A = 2.5$), the relationship of hot-electron energy deposition to the propagated areal density is presented in Fig. 4. The monoenergic hot electron with an energy of 100 keV is reported to have a stopping range of $\sim 15$ mg/cm$^2$ in DT plasma.[11] Excellent agreement of 15 mg/cm$^2$ areal density is obtained in our hot-electron package. The locally deposited flux is also shown in Fig. 4. As the hot electron propagates into the plasma (the outside surface of the target), the plasma density increases and many more binary collisions occur; also more scattering occurs and more hot-electron energy is deposited locally. As a result, the initial monoenergetic 100-keV hot electron decreases continuously down to zero, and the locally deposited flux increases continuously until the hot-electron propagation range.

## 3. Gain characteristics of electron-driven shock ignition

The shock-ignition target on the NIF was designed[24] and utilized to propose the electron-driven shock ignition scheme.[9] The laser pulse is separated into two parts, including the low laser intensity compressed pulse $\sim 5\times10^{14}$ W/cm$^2$ which provides the low velocity $\sim 200$ km/s and low adiabats $\sim 1.8$ compression, and the high laser intensity spike $\sim 3.4\times10^{15}$ W/cm$^2$ with a duration of $\sim 200$ ps, which provides an ignitor shock about hundreds Mbar. The launching time of the high intensity laser spike is varied in this work. An earlier launching time implies a less compressed target and an earlier ignitor shock. The gain of every implosion is measured versus the high-intensity laser spike launching time and is presented in Fig. 5. The highest gain of $\sim 40$ was obtained with an ignitor shock launching time of 9.6 ns. In shock ignition, if the ignitor shock is launched too early in time, the incoming strong shock could transmit the inside surface of the moving shell and collide with the outcoming shock in the low-density hot spot. In this case there will be no secondary shell piston effect, which is the main problem of shock ignition. The stagnation hot spot will be low and there will be no ignition. Conversely, if the ignitor shock is launched too late, it will collide with the outcoming return shock near the shell's outside surface. In this case, the collision may be close to the stagnation time, which does not help the ignition. Additionally, there will be a divergent shock after the collision, and it will transmit the outside shell surface quickly and induces a rarefaction wave which will decompress the shell and decrease the ignition. As a result, there is an ignition window for the ignitor shock launching time.[30] When delivered right on time, the ignitor shock collides with the return shock close to the inner shell surface. A 250-ps ignition window was observed in this NIF shock-ignition target design by LILAC; there is an ignition cliff $\sim 9.7$ ns because in the optimized target design, the outcoming and incoming shocks collide near the inner surface of the shell.

The hot-electron-driven shock ignition gains *versus* ignitor launching times are also demonstrated in Fig. 5. A 200-ps hot-electron spike was used in the present study with Maxwellian energy distribution. The hot electron temperature was set at 60 keV according to the recent OMEGA experimental data.[19] As can be seen, the target did not ignite for a hot-electron energy of less than 10 kJ. For a laser power of 500 TW, the 10-kJ hot-electron spike with 200-ps duration has a laser to hot-electron energy conversion efficiency of $\sim 10\%$. As the hot-electron energy increases, the target ignites. A highest gain of $\sim 27$ is achieved within the hot-electron energy of 15 kJ, which has a laser to hot-electron energy conversion efficiency of $\sim 15\%$. The instantaneous

laser to hot-electron energy conversion efficiency was measured to be 15% on OMEGA with a CH target and with no smoothing by spectral dispersion (SSD).[19] Within NIF shock ignition, the laser intensity does not change compared to the OMEGA design, and the laser pulse duration could be $\sim 4\times$ as that on OMEGA according to the hydrodynamic equivalence scaling.[15] As a result, the NIF shock-ignition plasma scale should be $\sim 4\times$ as that on OMEGA, which implies that much more hot-electron energy can be obtained on an NIF-scale plasma. If a laser to hot-electron energy conversion efficiency of $\sim 25\%$ ($\sim 25$ kJ) is adopted in DEC2D simulations, implosions with a gain over 100 can be obtained. An $\sim 500$-ps ignition window is achieved, which means that more hot-electron energy can tolerate more shock mistiming, and more robust ignition is obtained within the hot-electron-driven shock ignition scheme.

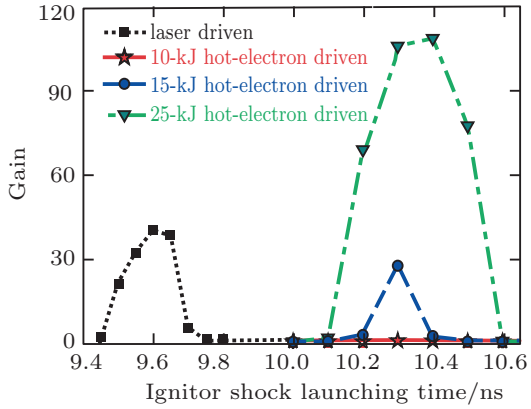



**Fig. 5.** The gains versus the ignitor shock launching times. The black line represents LILAC calculations with the laser-driven shock ignition, and the colored lines are 1D simulations with the hot-electron-driven shock ignition with different hot-electron energies.

## 4. Optimum implosion of electron-driven shock ignition

The ignitor shock strength is one of the most important parameters of shock ignition. Different ignitor shock launching schemes have different ignitor shock properties and can lead to different implosion characteristics. In this work, the laser spike-driven ignitor shocks and the hot-electron spike-driven ignitor shocks are presented in Fig. 6. The laser-driven ignitor shock is chosen as the highest gain $\sim 40$ of the LILAC target design, which is shown in Fig. 5 at the laser spike launching time of 9.6 ns. The hot-electron-driven ignitor shock is chosen as the highest gain $\sim 106$ of DEC2D simulations, which is also shown in Fig. 5 at the hot-elelctron spike launching time of 10.3 ns. The laser energy is deposited in the corona zone until the critical density $n_c = 1.1\times 10^{21}/\lambda^2$ cm$^{-3}$,[31] where $\lambda_{\mu m}$ is the laser wavelength in unit of μm, and most of laser energy is deposited near the critical surface. As a result, the laser-driven shock is launched near the critical surface. As for the specific target design with a laser spike launching time of 9.6 ns, a high-intensity laser $\sim 3.4\times 10^{15}$ W/cm$^2$ launches a 0.1-Gbar shock after 100 ps, which is shown in Fig. 6(b). The incoming strong shock continues to compress the shell, propagates toward the target center, and rises to 0.2 Gbar after 200 ps, which is shown in Fig. 6(c).

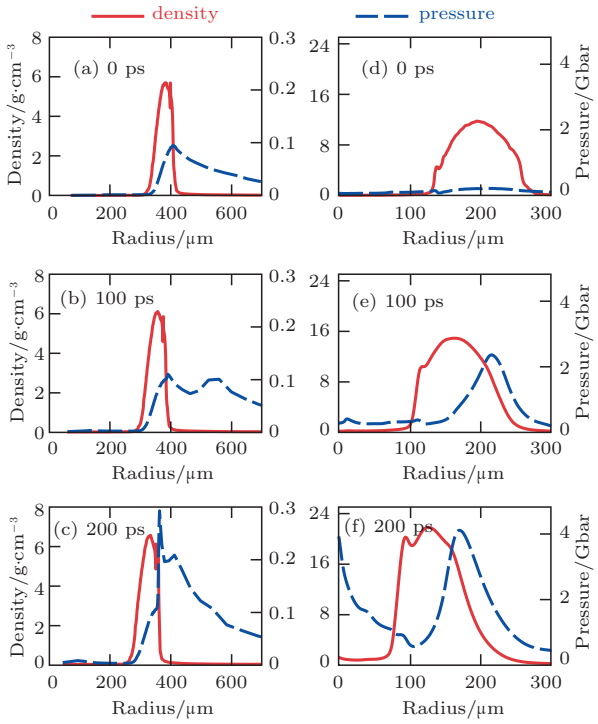



**Fig. 6.** The density and pressure profiles after the ignitor shock launched for 0, 100, and 200 ps. Panels (a)–(c) for the laser spike driven, and panels (d)–(f) for the hot-electron spike driven. The highest gain targets in Fig. 5 are utilized. For the laser-driven shock ignition, the ignitor shock launching time is 9.6 ns, and for the hot-electron-driven shock ignition, the ignitor shock launching time is 10.3 ns.

For the hot-electron-driven case, the hot electrons are generated in the corona zone and depend on the non-linear lPI processes. For instance, if TPD is dominated, most of the hot electrons are produced in $n_c/4$, which is the same as that on OMEGA direct-drive implosions. If SRS is dominated, the hot electrons are produced in some specific areas of corona, which depends on the plasma parameters and noise levels, and the SRS dominated nonlinear LPI process occurs in the high laser intensity (shock-ignition relevant) experiments, as performed recently on OMEGA.[19] However, no matter where exactly the hot electrons generated, the propagation range of hot electrons is large and the corona plasma is not massive enough to stop the hot electrons. The hot electrons transport directly into the high-density shell, and a 2.4-Gbar shock is formed on the outside surface of the shell after 100 ps, which is shown in Fig. 6(e). A 4.1-Gbar strong shock is generated after 200 ps, which is shown in Fig. 6(f). The isothermal rarefaction model can be used to analyze the corona plasma, and the laser-driven ablation pressure is reported to be $P = 40(I_{15}/\lambda)^{2/3}$.[32] The hot-electron-driven ablation pressure can be written as $P = 175\rho^{1/3}(I_{15}\eta)^{2/3}$.[11] For $\lambda_{\mu m} = 351$ nm, the ratio of the

hot-electron-driven ablation pressure to the laser-driven ablation pressure can be obtained as $2.17\rho^{1/3}\eta^{2/3}$. From this simple model, for $\eta = 25\%$, the plasma density of $\rho = 1.6$ g/cm$^3$ can generate the same strength shocks for the laser- and hot-electron-driven cases. At the hot-electron launching time of 10.3 ns, the maximum shell density is 12 g/cm$^3$, which means a 1.94× shock can be generated in the hot-electron-driven shock ignition compared to that of the laser-driven shock ignition. However, the above analysis is based on simple planar analytical models. Considering all the physical mechanisms and spherical geometry, DEC2D simulations observe $\sim 20\times$ enhancements for the hot-electron-driven shock compared to the laser-driven shock at both 100 ps and 200 ps, which can be seen in Fig. 6.

The ignitor shock compresses the shell and the center low-density gas region, which is called the "hot spot". The pressure of the hot spot keeps increasing because of the geometry convergence, the shock transmission, and the mass increase from the ablation of the inner surface of the low-temperature, high-density shell. When the hot-spot pressure equals the shell pressure, the acceleration phase ends, the shell velocity starts to decrease, and the deceleration phase comes out. For the laser-driven shock ignition with a laser launching time of 9.6 ns, the trajectory of the shell peak density and the shell velocity are presented in Fig. 7(a). There is a peak density location jump at around 9.8 ns toward the outside surface, which is caused by the laser-driven shock catching up with the outside shell surface [see Fig. 6(c)], this jump compresses the outside part of the shell into a high density. The laser pulse turns off at 9.8 ns, but the shell velocity keeps increasing from 9.8 ns to 10.6 ns, owing to the compression by the hot-spot pressure to the inside part of the shell. The mass center moves toward the target center. At 10.6 ns, there is a sudden enhancement in the shell velocity from 284 km/s to 294 km/s because the incoming and outcoming shocks collide. During this process a very high density zone ($\sim 3\times$ that of the density before collision) can be generated near the inner surface of the shell.

The mass center trajectory and shell velocity of the electron-driven shock ignition with the ignitor shock launching time of 10.3 ns are shown in Fig. 7(b). The stagnation occurs at about 10.8 ns, which is the same for the laser-driven shock ignition in Fig. 7(a). The time duration from the ending of the hot-electron spike to the stagnation is $\sim 300$ ps, which is $\sim 1/3$ of that in the laser-driven shock ignition. The reason is that the hot-spot pressure is comparable to the shell pressure in the hot-electron-driven shock ignition when the hot-electron spike turns off, and the hot-spot pressure is negligible in comparison with the shell pressure in the laser-driven shock ignition when the laser spike turns off. As a result, it takes less time for the hot-electron-driven shock ignition to achieve an equivalent result between the hot spot and the shell, and it implies less perturbation growth in the deceleration phase, which benefits the implosion performance. At 10.6 ns, a similar sudden enhancement of the shell velocity is observed within the electron shock ignition because of the collision of the incoming and outcoming shocks. However, the shell velocity increases from 385 km/s to 484 km/s, which has more shell velocity enhancement than that of the laser-driven shock ignition (from 284 km/s to 294 km/s). It implies that more intense shock collision occurs and stronger incoming shock can be generated after the collision in the hot-electron-driven shock ignition, which benefits the second piston compression effect of the hot spot. The shell velocity at the end of the laser spike is 250 km/s and the maximum shell velocity (just after the collision) is 294 km/s, and the corresponding shell velocities of the hot-electron-driven shock ignition are 338 km/s and 484 km/s.

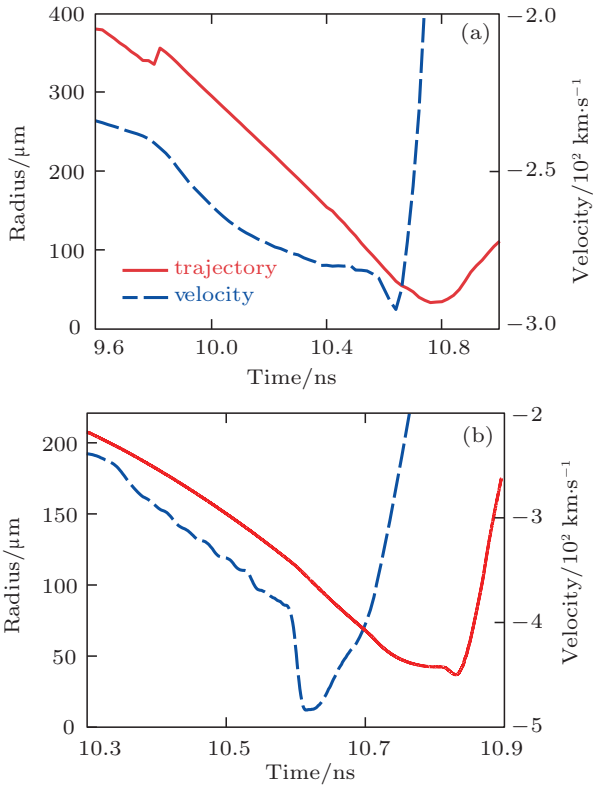



**Fig. 7.** The trajectory and implosity velocity for (a) the laser-driven shock ignition and (b) the hot-electron-driven shock ignition.

In an implosion, the thermonuclear instability is triggered in the central hot spot. Nuclear reactions occur in the hot spot with a cross section, and self-ignition occurs when $\rho R \geq 0.3$ g/cm$^2$ and $T_i \geq 5$ keV in the hot spot. The ignition products includes high-energy $\alpha$ particles and neutrons. The $\alpha$ particles form a burning wave toward the outside low-temperature and high-density shell, and deposits energy in the shell depending on the shell's areal density and temperature. In simulations, the burn-wave effect is not always considered and the $\alpha$ particles are turned off to investigate the pure hydrodynamic of the implosion. In Fig. 8, the stagnation pa-

rameters of the laser-driven shock ignition with a laser spike launching time of 9.6 ns, and the hot-electron-driven shock ignition with a hot-electron spike launching time of 10.2 ns are demonstrated with $\alpha$ particles turned off. The density profiles in Fig. 8(a) show that the shell density of the laser-driven shock ignition at stagnation is greater than that of the hot-electron-driven shock ignition. However, the hot-spot density of the laser-driven shock ignition ($\sim 93$ g/cm$^3$ in the target center) is less than that of the hot-electron-driven shock ignition ($\sim 144$ g/cm$^3$ in the target center). The shell thickness of the laser-driven shock ignition is less than that of the hot-electron-driven shock igniton with both of the two cases having almost the same outside shell surface. The hot-spot pressure of the laser-driven shock ignition (378 Gbar in the target center) is much less than that of the hot-electron-driven shock ignition (644 Gbar in the target center). It has been shown above that the hot-electron-driven shock ignition implosion has greater shell velocity compared to that of the laser-driven shock ignition, which implies that greater hot-spot pressure can be achieved within the hot-electron-driven shock ignition, according to the scaling law[14]

$$\langle P\rangle \approx \frac{345}{\alpha^{0.9}}\left[\frac{V_{\rm i}}{3\times 10^7}\right]^{1.85}.$$

The hot-spot boundary at stagnation is set as the ion temperature $T_{\rm i} \sim 1$ keV in this work. For the laser-driven shock ignition $R_{\rm s} \sim 27$ μm, and for the hot-electron shock ignition $R_{\rm s} \sim 25.5$ μm. According to the adiabat compression model, a $PR^5 =$ const scaling can be derived from the hot-spot energy equation by neglecting the thermal conduction and the $\alpha$-particle energy deposition. As a result, the ratio of the stagnation hot-spot pressure of the hot-electron-driven shock ignition to that of the laser-driven shock ignition can be written as $P_{\rm hot}/P_{\rm laser} \sim (27/25.5)^5 = 1.3$, which is less than that shown in Fig. 8(b) as $P_{\rm hot}/P_{\rm laser} \sim 644/378 = 1.7$. This discrepancy implies that it is not adiabat compression in the hot-spot dynamics, and other mechanisms should be considered. The hot-spot masses are calculated, and $m_{\rm hs} \sim 16.1$ μg in the laser-driven shock ignition, $m_{\rm hs} \sim 26.7$ μg in the hot-electron-driven shock ignition. With the initial gas mass of 0.66 μg in the target design, 24× and 40× hot-spot mass increases are achieved in the laser-driven and the hot-electron-driven shock ignitions respectively. In the hot-electron-driven shock ignition, more than 10 μg shell material mass is ablated into the hot spot, leading to an increase in the hot-spot pressure. The ion temperature profiles presented in Fig. 8(c) do not demonstrate a great difference for the laser- and hot-electron-driven shock ignitions. In the hot-electron shock ignition, the higher shell velocity leads to a higher hot-spot temperature, but much more ablation to the cold shell's inner surface occurs, and much more cold shell mass comes into the hot-spot and decays the hot spot temperature. The adiabat profiles of the laser- and hot-electron-driven shock ignitions are shown in Fig. 8(d). The adiabat of the laser-driven shock ignition (the minimum is $\sim 1.95$) is less than that of the hot-electron-driven shock ignition (the minimum is $\sim 2.55$). This is because the laser energy is deposited in the corona and the hot-electron energy is deposited about half peak density at the outside shell surface. The greater propagation range of the hot electron leads to the higher adiabat in the hot electron shock ignition and broadens the shell, which is shown in Fig. 8(a).

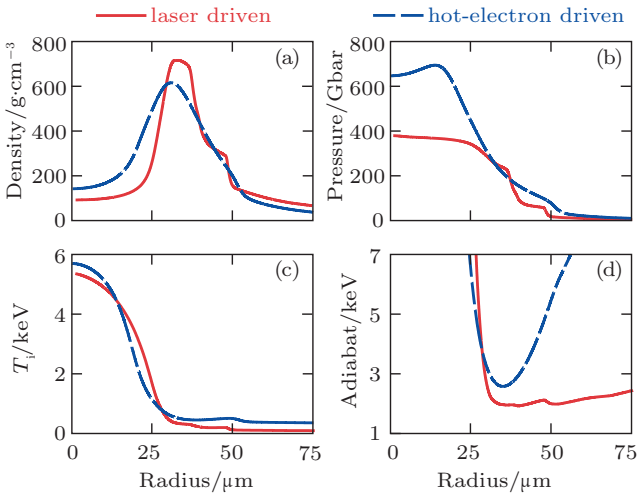



**Fig. 8.** The target density profile (a), pressure profile (b), temperature profile (c), and adiabat profile (d) at stagnation without burn wave for the laser- and hot-electron-driven shock ignitions.

The evolutions of the neutron rate in the laser- and hot-electron-driven shock ignitions with burn wave are shown in Fig. 9(a). The confinement time of the ignition implosion can be written as $\tau \sim R_{\rm s}/c_{\rm s}$, where $R_{\rm s}$ is the hot-spot radius and $c_{\rm s}$ is the sound speed of the burn wave at the peak neutron rate. For the laser-driven shock ignition, $\tau \sim 40$ ps; for the hot-electron-driven shock ignition, $\tau \sim 23$ ps. However, the peak neutron rate is greater for the hot-electron-driven shock ignition than that for the laser-driven shock ignition. The peak neutron rate along with the density, pressure, and ion temperature profiles are presented in Figs. 9(b)–9(d). At peak neutron rate, the hot-spot density for the laser-driven shock ignition is 74 g/cm$^3$, and for the hot-electron-driven shock ignition is 165 g/cm$^3$. The hot-spot pressure for the laser-driven shock ignition is 1672 Gbar, and for the hot-electron-driven shock ignition is 5172 Gbar. The ion temperature profiles for the laser- and hot-electron-driven shock ignitions are almost the same in Fig. 9(d). In the electron shock ignition, more cold shell material is ablated into the high temperature hot-spot, which increases the hot-spot density and pressure, and degrades the hot spot temperature.

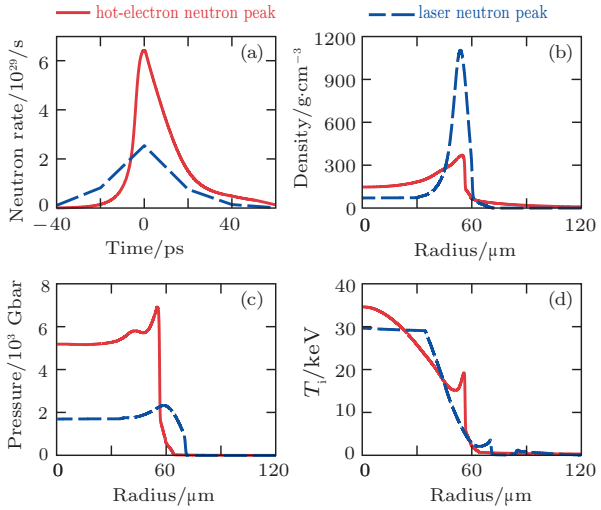



**Fig. 9.** (a) The neutron rate, (b) target density profile, (c) pressure profile, (d) and ion temperature profile at peak neutron rate with burn wave for the laser- and hot-electron-driven shock ignitions.

## 5. Conclusions

The hot-electron energy deposition in plasma depends on the hot-electron energy and the material density. In a planar target, for a laser to hot-electron energy conversion efficiency of 25%, greater ablation pressure can be obtained by the hot-electron-driven than that by the laser driven with plasma density greater than 1.6 g/cm$^3$. In our spherical 1D simulations, 20× pressure enhancement is obtained by the hot-electron-driven shock ignition compared to that by the laser-driven shock ignition. The hot-electron-driven scheme can be much more effective than the laser-driven scheme with suitable hot-electron energy and plasma density.

In this work, the Solodov–Betti hot-electron stopping power model was utilized, binary collisions including electron–electron and electron–ion collision and exciting plasma waves effect were considered, the Lewis' multiple scattering theory was used to calculate the spatial moments of the hot-electron energy deposition. According to the recent OMEGA experiment data, the hot-electron temperature of 60 keV was used in our simulations. More than 2 Gbar of shock was generated in our work within the suitable hot-electron spike launching time. The hot-electron shock ignition can obtain greater shell velocity than that of the laser-driven shock ignition, which implies more hot-spot pressure in the deceleration phase, and more gain in the implosion. The hot-spot temperature profiles of the laser- and hot-electron-driven shock ignition are almost the same, the reason being that greater shell velocity in the hot-electron shock ignition leads to higher hot-spot temperature, and it also ablates more inner surface of the cold shell into the hot spot and decreases the hot-spot temperature. In the simulations more than 10-μg shell mass was ablated into the hot spot in the hot-electron shock-ignition than that in the laser-driven shock ignition, and the ablated mass into the hot spot increased the hot-spot density and pressure and also decreases the hot-spot temperature. On the other side, the hot electron can propagate deeper than the laser, and it leads to a higher adiabat for the shell in the hot-electron driven shock ignition than that of the laser-driven shock ignition, which broadens the shell and degrades the shell areal density. However, the increased shell velocity can surmount the degradation of the shell areal density caused by the increase of the adiabat in the hot-electron-driven shock ignition. The hot-electron-driven shock ignition can be a robust (big ignition window), high gain ($> 100$) ignition scheme in ICF.

The self-generated electromagnetic field is not taken into considered in these 1D simulations. Three-dimensional (3D) extended-magnetohydrodynamic simulations have proved that the electromagnetic fields lead to significant distortions to the plasmas temperature and density, which degrade the implosion performance.[33] It should be pointed out that the self-generated electromagnetic field needs to be considered in future 2D/3D simulations about the hot electron shock ignition scheme. Additionally, The straight line model of the hot electron deposition is utilized in our simulations, and the hot electron transport diffusion, the hot electron refraction and reflection in the plasma could be the future work.

## References

[1] Cai H B, Mima K, Zhou W M, Jozaki T, Nagatomo H, Sunahara A and Mason R J 2009 *Phys. Rev. Lett.* **102** 245001
[2] Theobald W, Betti R, Stoeckl C, Anderson K S, Delettrez J A, Glebov V Yu, Goncharov V N, Marshall F J, Maywar D N, McCrory R L, Meyerhofer D D, Radha P B, Sangster T C, Seka W, Shvarts D, Smalyuk V A, Solodov A A, Yaakobi B, Zhou C D, Frenje J A, Li C K, Séguin F H, Petrasso R D and Perkins L J 2008 *Phys. Plasmas* **15** 056306
[3] Betti R, Zhou C D, Anderson K S, Perkins J L, Theobald W and Solodov A A 2007 *Phys. Rev. Lett.* **98** 155001
[4] Atzeni S, Marocchino A, Schiavi A and Schurtz G 2013 *New J. Phys.* **15** 045004
[5] Shang W, Wei H, Li Z, Yi R, Zhu T, Song T, Huang C and Yang J 2013 *Phys. Plasmas* **20** 102702
[6] Lafon M, Ribeyre X and Schurtz G 2013 *Phys. Plasmas* **20** 022708
[7] Perkins L J, Betti R, LaFortune K N and Williams W H 2009 *Phys. Rev. Lett.* **103** 045004
[8] Canaud B and Temporal M 2010 *New J. Phys.* **12** 043037
[9] Shang W L, Betti R, Hu S X, Woo K, Hao L, Ren C, Christopherson A R, Bose A and Theobald W 2017 *Phys. Rev. Lett.* **119** 195001
[10] Gus'kov S, Ribeyre X, Touati M, Feugeas J L, Nicola Ph and Tikhonchuk V 2012 *Phys. Rev. Lett.* **109** 255004
[11] Ribeyre X, Gus'kov S, Feugeas J L, Nicola Ph and Tikhonchuk V T 2013 *Phys. Plasmas* **20** 062705
[12] Piriz A R, Piriz S A and Tahir N A 2013 *Phys. Plasmas* **20** 112704
[13] Campbell E M and Hogan W J 1999 *Plasma Phys. Control. Fusion* **41** B39
[14] Zhou C D and Betti R 2007 *Phys. Plasmas* **14** 072703
[15] Nora R, Betti R, Anderson K S, Shvydky A, Bose A, Woo K M, Christopherson A R, Marozas J A, Collins T J B, Radha P B, Hu S X, Epstein R, Marshall F J, McCrory R L, Sangster T C and Meyerhofer D D 2014 *Phys. Plasmas* **21** 056316
[16] Kirkwood R K, Moody J D, Kline J, Dewald E, Glenzer S, Divol L, Michel P, Hinkel D, Berger R, Williams E, Milovich J, Yin L, Rose H, MacGowan B, Landen O, Rosen M and Lindl J 2013 *Plasma Phys. Control. Fusion* **55** 103001

[17] Seka W, Edgell D H, Myatt J F, Maximov A V, Short R W, Goncharov V N and Baldis H A 2009 *Phys. Plasmas* **16** 052701

[18] Kemp A J, Fiuza F, Debayle A, Johzaki T, Mori W B, Patel P K, Sentoku Y and Silva L O 2014 *Nucl. Fusion* **54** 054002

[19] Theobald W, Nora R, Seka W, Lafon M, Anderson K S, Hohenberger M, Marshall F J, Michel D T, Solodov A A, Stoeckl C, Edgell D H, Yaakobi B, Casner A, Reverdin C, Ribeyre X, Shvydky A, Vallet A, Peebles J, Beg F N, Wei M S and Betti R 2015 *Phys. Plasmas* **22** 056310

[20] Solodov A A and Betti R 2008 *Phys. Plasmas* **15** 042707

[21] Li C K and Petrasso R D 2006 *Phys. Rev. E* **73** 016402

[22] Reik H G and Risken H 1961 *Phys. Rev.* **124** 777

[23] Delettrez J, Epstein R, Richardson M C, Jaanimagi P A and Henke B L 1987 *Phys. Rev. A* **36** 3926

[24] Anderson K, Betti R and Gardiner T A 2001 *Bull. Am. Phys. Soc.* **46** 280

[25] Bose A, Woo K M, Nora R and Betti R 2015 *Phys. Plasmas* **22** 072702

[26] Woo K M, Betti R, Bose A, Epstein R, Delettrez J A, Anderson K S, Yan R, Chang P Y, Jonathan D and Charissis M 2015 presented at the 57*th Annual Meeting of the APS Division of Plasma Physics*, Savannah, GA, 16–20 November, 2015 (GO5.00003) (unpublished)

[27] Anderson K S, Betti R, McKenty P W, Collins J B, Hohenberger M, Theobald W, Craxton R S, Delettrez J A, Lafon M, Marozas J A, Nora R, Skupsky S and Shvydky A 2013 *Phys. Plasmas* **20** 056312

[28] Goncharov V N, Sangster T C, Boehly T R, Hu S X, Igumenshchev I V, Marshall F J, McCrory R L, Meyerhofer D D, Radha P B and Seka W 2010 *Phys. Rev. Lett.* **14** 165001

[29] Lewis H W 1950 *Phys. Rev.* **78** 526

[30] Ribeyre X, Schurtz G, Lafon M, Galera S and Weber S 2009 *Plasma Phys. Control. Fusion* **51** 015013

[31] Shang W, Yang J and Dong Y 2013 *Appl. Phys. Lett.* **102** 094105

[32] Lindl J 1995 *Phys. Plasmas* **2** 3933

[33] Walsh C A, Chittenden J P, McGlinchey K, Niasse N P L and Appelbe B D 2017 *Phys. Rev. Lett.* **118** 155001